Chemical Engineering Journal 447 (2022) 137332

Contents lists available at ScienceDirect

Chemical Engineering Journal

journal homepage: www.elsevier.com/locate/cej

Hydrogen peroxide-impregnated supramolecular precursors synthesize mesoporous-rich ant nest-like filled tubular g-C_3N_4 for effective photocatalytic removal of pollutants

Ting Wu [a], Zhifeng Liu [a,*], Binbin Shao [a], Qinghua Liang [a], Qingyun He [a], Yuan Pan [a], Xiansheng Zhang [a], Yang Liu [a], Jingwen Sun [a], Shanxi Gong [b]

[a] College of Environmental Science and Engineering, Hunan University and Key Laboratory of Environmental Biology and Pollution Control (Hunan University), Ministry of Education, Changsha 410082, PR China
[b] School of Chemistry and Chemical Engineering, Guangxi University, Nanning 530004, PR China

ARTICLE INFO

Keywords:
Supramolecule
Photocatalysis
Mesoporous filling
Tubular g-C_3N_4
Theoretical calculation

ABSTRACT

The problem that the hollow part with macroporous size in the hollow tubular g-C_3N_4 is difficult to function in photochemical reactions has been neglected for a long time. To address this issue, tubular g-C_3N_4 with mesoporous-rich non-hollow ant nest-like filling (AN-TCN) was prepared by calcining supramolecular precursors impregnated with hydrogen peroxide solution. The endogenous gas released from the wet rod-like supramolecular precursor during thermal polymerization contributed to the construction of a mesoporous filling structure inside the AN-TCN, which not only increased the reactive sites, but also enhanced the ability of visible light response and facilitated the separation and transfer of photoinduced charges. Experiments and theoretical calculations were conduct together to reveal the physicochemical characteristics of AN-TCN. The photocatalytic capacity of AN-TCN-4.5 for tetracycline hydrochloride (TCH) reached to 86 % under visible radiation within 30 min. This study afforded a new thinking and strategy for morphology regulation and performance optimization of g-C_3N_4-based photocatalyst.

1. Introduction

The environmental problems are closely connect with the life of human beings and all kinds of animals and plants [1]. A healthy ecological environment contributes to the sustainable development of human society, so environmental protection and restoration cannot be ignored during social development [2–4]. As a kind of effective therapeutic drugs, antibiotic has been widely applied in the fields of healthcare, breeding industry and stock farming and others. Then a large amount of residual antibiotics enters the ecological environment through excretion or metabolism, which may cause biological aberrations and even produce resistance genes, which seriously threatening the health of the ecosystem [5–7]. In order to solve this problem, it is necessary to explore an effective method that can rapidly degrade antibiotics to reduce their accumulation in the environment, and thus to alleviate their threats to the ecosystem. Ascribing to photocatalysis is an advanced oxidation technology that uses solar energy as a driving force, its sustainability and low-cost characteristics make it an effective and considerable technology for environmental remediation [8]. The development of photocatalysts with high catalytic performance, strong stability and low cost is the key to advancing this technology to practical applications.

As a metal-free semiconductor, graphitic carbon nitride (g-C_3N_4) possesses an ideal band gap (about 2.6 ~ 2.9 eV), stable physical–chemical properties, cheap raw materials, and simple preparation process etc., making it an ideal photocatalyst [9,10]. Nevertheless, due to the low photo-generated carriers separation, weak visible light responsiveness and limited specific surface area, the photocatalytic performance of the initial g-C_3N_4 need to be further promoted [11]. Therefore many measures such as element doping [12,13], building defects [14], constructing heterojunction [15,16], etc. have been conducted to improve the photoelectric property of g-C_3N_4. Especially, in the past five years, a large number of researches on composite g-C_3N_4-based photocatalysts have been spawned, including binary composites [17], ternary composites [18], and even quaternary composites [19,20]. However, due to the poor stability and difficulty in the preparation of

* Corresponding author.
E-mail address: zhifengliu@hnu.edu.cn (Z. Liu).

https://doi.org/10.1016/j.cej.2022.137332
Received 17 March 2022; Received in revised form 13 May 2022; Accepted 30 May 2022
Available online 2 June 2022

multi-component photocatalysts, its development is gradually restricted. On the contrary, recently, synthesis of monomer g-C_3N_4 attracts the attention of researchers again due to its simple preparation process and high stability. For example, Zhou et al. prepared the monomer g-C_3N_4 nanotubes grafted with hydroxyl groups on its surface to promote the photocatalytic production of hydrogen peroxide [21]. Jiang et al. also obtained functionalized monolayer g-C_3N_4 with high photocatalytic hydrogen production ability through low boiling point solvent mediation [22].

In addition, some other methods such as the morphology, size and crystallinity adjustment were also used to improve the physicochemical properties of g-C_3N_4 [23]. To date, g-C_3N_4 with different dimensions include the 0D quantum dots [24], 1D nanofibers and nanotubes [25], 2D nanosheets [26], and 3D nanospheres and nanoflower [27] have been reported. Among these structures, benefiting from the characteristics of hollowness, porousness and resistance to agglomeration, the 1D tubular g-C_3N_4 exhibits an ideal specific surface area and exposes numerous reaction sites, which is contributed to its excellent photocatalytic property [28]. Therefore, the study of tubular g-C_3N_4 has been favored by many researchers. The main methods for synthesizing tubular g-C_3N_4 include thermal polymerization [28,29], template method [30], and self-assembly [31] etc., which were often conducted in harsh conditions and cumbersome steps or even need the strong acid or strong base mediation and multi-component adjustment, etc. [25,31–33]. Furthermore, the tubular g-C_3N_4 obtained by the above methods usually has a thick tube wall or a completely hollow structure, which made it difficult to function due to the large pore diameter and lacked specific surface area, resulting in a waste of internal space. Consequently, building a mesoporous-rich structure in the tubular g-C_3N_4 and improve the specific surface area and reactive sites is necessary. A feasible method to increase the porosity was to release a large amount of endogenous gas during the thermal polymerization process, and subsequently promoted the construction of porous structure by the impact force of gas escape. Therefore, it is conceivable that the preparation of porous tubular g-C_3N_4 can be achieved by inserting a gas-releasing substance into the tubular g-C_3N_4 precursor prior to calcination.

Herein, inspired by the characteristics mentioned above, synthesis of tubular g-C_3N_4 precursors and selection of gas releasing substrates are the preconditions to synthesize monomer multi-mesoporous tubular g-C_3N_4. Fortunately, a simple and effective method for synthesizing tubular precursors by supramolecular self-assembly of melamine and its hydrolysates has been reported by our group [34]. Then although many substances can release gases at high temperatures, such as carbonates, nitrates, etc., these substances may produce greenhouse gases and even toxic nitrogen-containing gases. Therefore, the hydrogen peroxide (H_2O_2) solution that not only can be embedded in the precursor material but also will not generate polluting gas was chosen as the substance for endogenous gas releasing to generate a large amount of gas by the decomposition of H_2O_2 and vaporization of H_2O molecules, which were released from the inside out during the thermal polymerization process. Subsequently, the precursor was shocked by the endogenous gas during the thermal polymerization process and generated a mesoporous-rich structure in the tubular g-C_3N_4 (Scheme 1). In addition, due to the higher humidity of the tubular precursor after impregnation of H_2O_2 solution, the high degree of polymerization inside the precursor was inhibited, thus to obtain an ant nest-like filled tubular g-C_3N_4 (AN-TCN) with a layered stacked mesoporous-rich filling structure. This made up for the defect that the internal structure of the completely hollow tubular g-C_3N_4 was underutilized. The ant nest-like filling increased the reactive sites of the prepared materials and improved the photochemical performance for AN-TCN. In addition, the oxygen atom originated from the decomposition of H_2O_2 during thermal polymerization would be doped in a small amount in the g-C_3N_4 structure, which not only played a role in adjusting the energy band, but also acted as an electron donor to provide electrons to surrounding atoms and constructed a polarizing electric field, thus facilitating the separation of photoinduced charges. Therefore, the prepared AN-TCN showed a better degradation capacity for tetracycline hydrochloride (TCH) than the initial CN and TCN. Furthermore, in order to further explore the influence of oxygen atoms on the electronic structure of AN-TCN, the DFT theoretical calculation and a variety of characterization techniques were combined to systematically explain the reasons for improved photocatalytic properties.

This study developed a simple method of preparing the internally filled tubular g-C_3N_4 monomer photocatalyst with high specific surface area and abundant reactive sites by calcining the supramolecular precursors impregnated with H_2O_2 solution and explained the reason for the formation of internal mesoporous filling. Besides, this work solved the problems of insufficient mesoporous structure and less reactive site of tubular g-C_3N_4 and afforded a novel thought and reference for the study of photocatalysis.

2. Experiment

2.1. Photocatalyst preparation

The supramolecular precursor was prepared firstly though a hydrothermal process. Detailly, 1.26 g melamine was put into 80 mL distilled water and dissolved to obtain a clear solution at 80 °C for 30 min. Followed transfer the mixed solution to a 100 mL Teflon liner and then hydrothermally heated in an autoclave for 10 h at 180 °C. After cooling, white crystals were collected by vacuum filtration and dried at 60 °C overnight to obtain the dry supramolecular precursor. Then, 500 mg supramolecular precursor was impregnated by 1 mL H_2O_2 solution of different mass fraction ratios (0, 1.5 %, 4.5 % and 9 %). Subsequently, the impregnated supramolecular precursors were directly put into crucibles with a lid and tightly wrapped by tin foil and polymerized at 550 °C in nitrogen atmosphere for 2 h at a heating rate of 5 °C min^{-1} in the tubular furnace (Scheme 1). The synthesized samples were named AN-TCN-0, AN-TCN-1.5, AN-TCN-4.5 and AN-TCN-9, respectively. The steps for preparation of untreated tubular g-C_3N_4 (TCN) was the same as that of AN-TCN samples but without H_2O_2 solution impregnation.

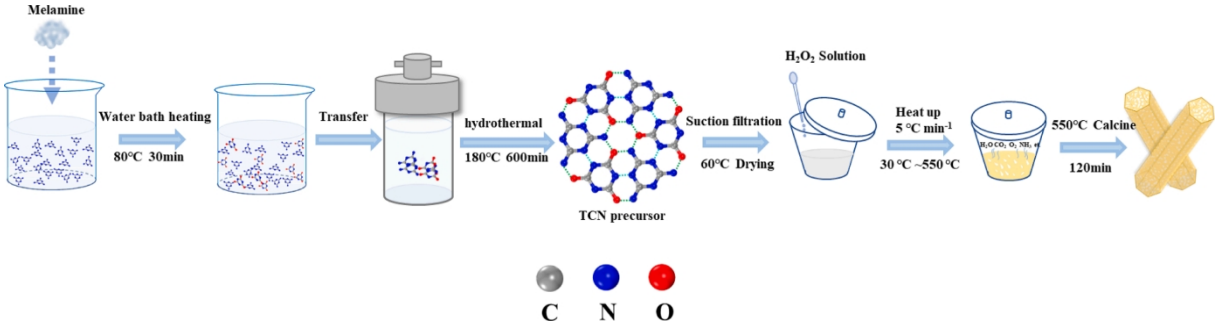

Scheme 1. Synthetic schematic diagram of AN-TCN.

Besides, to contrast with supramolecular precursors, melamine was also impregnated with 4.5 % H_2O_2 solution and then calcined under the same conditions to obtain HOCN. As for the traditional bulk g-C_3N_4 (CN) and porous bulk g-C_3N_4 (PCN), 3 g melamine and urea were thermally polymerized respectively under the same conditions as AN-TCN. Furthermore, the HDTCN-4.5 was obtained by impregnating 300 mg prepared TCN sample with 2 mL of 4.5 % H_2O_2 solution and calcining again.

2.2. Characterization and DFT calculations

The surface structure and morphology were observed though SEM and TEM. The pore properties were tested though Brunauer-Emmett-Teller (BET) method. The crystal structure was measured by an X-ray diffractometer. The surface functional groups and surface chemical states were detected by infrared spectrometer and X-ray photoelectron spectrometer, respectively. Then the optical properties were measure through an UV–vis spectrophotometer and fluorescence spectrometer. The electrochemical performance was tested in a three-electrode system and then a X-band Elexsys system spectrometer was used to investigate the electron spin resonance (ESR) single. The intermediate product identification and mineralization rate were detected by liquid chromatography-tandem mass spectrometry (LC-MS) and Total Organic Carbon Analyzer, respectively. DFT calculations were carried though the CASTEP method. More details on characterization techniques and theoretical calculation are documented in Supplementary Information.

2.3. Photocatalytic activity

The photocatalytic activity was appraised by degrading antibiotic, taking TCH as an example. The degradation experiment was carried out under a 300 W xenon lamp, and visible light was intercepted by a 420 nm cut-off filter. In detail, 20 mg of photocatalyst was put into 20 mL of TCH solution with a concentration of 10 mg·L^{-1} in a quartz glass reactor, followed by ultrasonic dispersion for 1 min to obtain a uniform solution. Next, the adsorption–desorption experiment was performed for 0.5 h in darkness to reach adsorption–desorption equilibrium. Subsequently, the photocatalytic degradation process was conducted for another 0.5 h under the visible light irradiation. Then 1 mL reaction solution was taken at an interval of 3 min and passed it through a 0.45 μm membrane filter to obtain a clarified solution. The content of TCH in the reaction solution was detected by a UV–vis spectrophotometer at the wavelength of 357 nm.

3. Results and discussions

3.1. Synthesis mechanism of mesoporous structures

In order to understand the formation process of the mesoporous-rich filling structure in AN-TCN, the morphological changes of the supramolecular precursors impregnated with 4.5 % H_2O_2 solution during thermal polymerization were investigated. At a heating rate of 5 ℃·min^{-1}, the changes of the samples and the degree of gas release were observed when the calcination temperature rose to 80 °C, 100 °C, 150 °C, 200 °C, 250 °C, 300 °C, 350 °C, and 400 °C. As shown in Fig. S1, after immersion with H_2O_2 solution, the supramolecular precursor was in a paste state (Fig. S1a). When the calcination temperature reached 80 ℃, no gas escaped and the sample remained paste state (Fig. S1b), indicating that the H_2O_2 aqueous solution did not evaporate or decompose at this time. As the temperature increased to 100 °C, a little gas evolution was observed, and the impregnated supramolecular precursor remained a paste (Fig. S1c). When the temperature increased to 150 ℃, the degree of gas release was enhanced, and the sample changed from the original paste to a cream with less water (Fig. S1d). The gas produced at this time not only contained the vaporized H_2O, but also contains H_2O and O_2 generated by the decomposition of H_2O_2, which due to H_2O_2 could be rapidly decomposed at about 150 °C. Then, when the calcination temperature reached 200 ℃~250 ℃, the gas was released violently, and the shape of the creamy sample began to solidify (Fig. S1e-f). And the pores on the surface of the cream was originating from the rapid escape of gas. As the calcination temperature rose to 300 °C, the impregnated supramolecular precursors were solidified and turned into a semi-dry powder, and gas evolution was significantly reduced (Fig. S1g). At the calcination temperature of 350 °C, fuming began to appear since the supramolecular precursors began to polymerize and gradually transform to g-C_3N_4 (Fig. S1h). At a higher polymerization temperature (400 °C), the supramolecular precursor continued to thermally polymerize and strongly released fumes, which might mainly compose of NH_3 and CO_2. At the same time, the sample turned from white to slightly yellowish (Fig. S1i). Subsequently, continued to heat to 550 ℃ and kept for two hours to obtain the pale yellow AN-TCN (Fig. S1j). At this time, the surface and interior of the sample were full of pores, which was due to the continuous escape of gas from the interior during the whole calcination process. It should be emphasized that the crucible containing the impregnated supramolecular precursor was sealed with a lid during calcination, which restrained the rapid escape of the released gas.

In addition, the mass loss of the impregnated supramolecular precursor during the calcination process with continuous temperature rise was shown in Fig. S2a. Except that the interval between 80 ℃ and 100 ℃ was 20 ℃, the interval between the other two adjacent points were 50 ℃. The results show that before 100 °C, there was only a very small amount of mass loss, which mainly corresponded to the evaporated some water molecules. Mass loss increased sharply between 100 ℃ and 250 ℃, which was consistent with the strong gas evolution observed in Fig. S1, that was the rapid vaporization of water and the decomposition of H_2O_2. Subsequently, the residual water molecules and H_2O_2 continue to evaporate and decompose at 250 ~ 300 ℃. After that, the supramolecular precursors gradually became dry and began thermal polymerization with slow mass loss at 300 ~ 350 ℃, which was determined in Fig. S2b, that the mass of the impregnated sample at 300 ℃ (0.9768 g) was less than the initial supramolecular precursors (1.0002 g). During the rapid heating process, the released O_2 that failed to escape in time in the relatively closed crucible would participate in the thermal polymerization process of the supramolecular precursor.

From the above observations, it could be seen that under the condition of rapid temperature rise, the gas generated by the vaporization and decomposition of H_2O_2 aqueous solution before 300 ℃ would be release continuously. And the released gas would not escape the crucible immediately due to the relatively airtight environment of the lidded crucible and thus to continuously flew and shuttled between the supramolecular precursors. During this process, the supramolecular layers in the supramolecular precursors would be impacted by vigorously moving gas, thereby promoting the construction of porous structures.

Furthermore, in order to explore the effect of H_2O_2 aqueous solution and gas evolution on the structure of supramolecular precursors, SEM images of the pristine precursors, water-impregnated precursors, and H_2O_2 solution-impregnated precursors at different calcination temperatures were observed. As shown in Figure S3a-c, after calcination at 100 ℃ for 2 h, all the precursors maintained a high degree of structural integrity, indicating that H_2O_2 would not break the structure of the supramolecular precursors. Meanwhile, the slow release of gas at this temperature did not affect the structure of the precursors. After being treated at 200 ℃, the original precursors still maintained a high degree of structural integrity, while the water-impregnated precursors and the H_2O_2 solution-impregnated precursors were slightly damaged due to the rapid release of gas (Fig. S3d ~ f). Subsequently, at 300℃, the initial precursors (Fig. S3g) still maintained a complete rod-like structure, while the degree of deformation of the precursors impregnated with H_2O_2 solution (Fig. S3i) was greater than that of the precursors impregnated with water (Fig. S3h), which was caused by the violent evaporation and decomposition of H_2O_2 solution at 200–300 ℃.

3.2. Morphology and pore characteristics

The morphology and structure of the obtained samples were observed though SEM and TEM. The traditional CN displayed a typically agglomerated bulk structure (Fig. 1a-b) and the pure TCN equipped with a regular hollow tube with a diameter of approximately 1 ~ 3 μm (Fig. 1c-d and Fig S4a). Differently, the inside of AN-TCN had an obvious filling of porous and orderly stacked lamellar structure, similar to the "ant nest" (Fig. 1e-f and Fig S4b-c), which might transform the original macroporous hollow tubular structure with diameter about 1 ~ 3 μm into a connected ant nest-like mesoporous-rich filling center, thereby increasing the specific surface area and reactive site and leading to the improvement of photocatalytic performance. The TEM elemental mapping indicated that in addition to C and N elements, O elements were also uniformly distributed in the AN-TCN, which might originate from the adsorbed oxygen species, or the O atoms doped in AN-TCN, which was supplied by the decomposition of H_2O_2 molecules in the impregnated supramolecular precursors during thermal polymerization (Fig. 1g).

To further verify the multi-mesoporous properties of AN-TCN, nitrogen adsorption isotherms about mesoporous were conducted (Fig. 2a). The type IV isothermal desorption curve and the type H3 hysteresis loop demonstrated that AN-TCN-4.5 was mainly contained mesoporous structure. And the curve of BJH pore size distribution (inset (a) in Fig. 2a) also showed the pore diameter was mainly distributed in the mesoporous region (2 ~ 50 nm), again indicating that the synthesized AN-TCN-4.5 mainly equipped with mesoporous structure. Besides, from the inset (b) in Fig. 2a, it could be seen that the pore volume of AN-TCN-4.5 was as high as 0.64 $cm^3\ g^{-1}$, which was 7.9 and 2.5 times of CN and TCN, respectively. And the AN-TCN-4.5 also possessed a large specific surface area of 93.9 $m^2\ g^{-1}$, which was 9.4 and 2.6 times that of CN and TCN, respectively. This result demonstrating that the ant nest-like filling center was composed of mesoporous structures, which increased the pore volume and specific surface area of AN-TCN-4.5, namely, providing more reactive sites, thus contributing to the improvement of the photocatalytic reaction efficiency. In addition, in order to demonstrate that the excellent photocatalytic and optoelectronic properties of AN-TCN benefited not only from its abundant mesoporous structure, but also from its unique filling structure, a bulk PCN with a porous structure was synthesized. As shown in Fig. S5, PCN and AN-TCN-4.5 had similar specific surface area and pore volume, which were 78.1 $m^2\ g^{-1}$ and 0.35 $cm^3\ g^{-1}$, respectively. And the specific surface area and pore volume of AN-TCN-4.5 were only 1.2 and 1.83 times that of PCN.

3.3. Crystal structure and surface characteristic

The crystal structure of prepared samples was investigated by XRD (Fig. 2b). Two typical diffraction peaks of AN-TCN-4.5 at 12.97° and 27.75° corresponding to the transversely extended (1 0 0) crystal planes and longitudinally stacked (0 0 2) crystal planes of g-C_3N_4, respectively. In comparison with the CN and TCN, the intensity of the two diffraction peaks of AN-TCN-4.5 were both decreased, which ascribed to the porous and loose structure inside the AN-TCN-4.5 inhibited the extension and crystallization of heptazine units on these two crystal planes. Then in order to explore the effects of H_2O_2 solution on the hollow tubular g-C_3N_4, the XRD of HDTCN-0.45 obtained by calcining the impregnated TCN with the 4.5 % H_2O_2 solution was also measured. Compared with TCN, there was no obvious difference in HDTCN-0.45 except for a slight decrease in the diffraction peak intensity of the (1 0 0) crystal plane. This

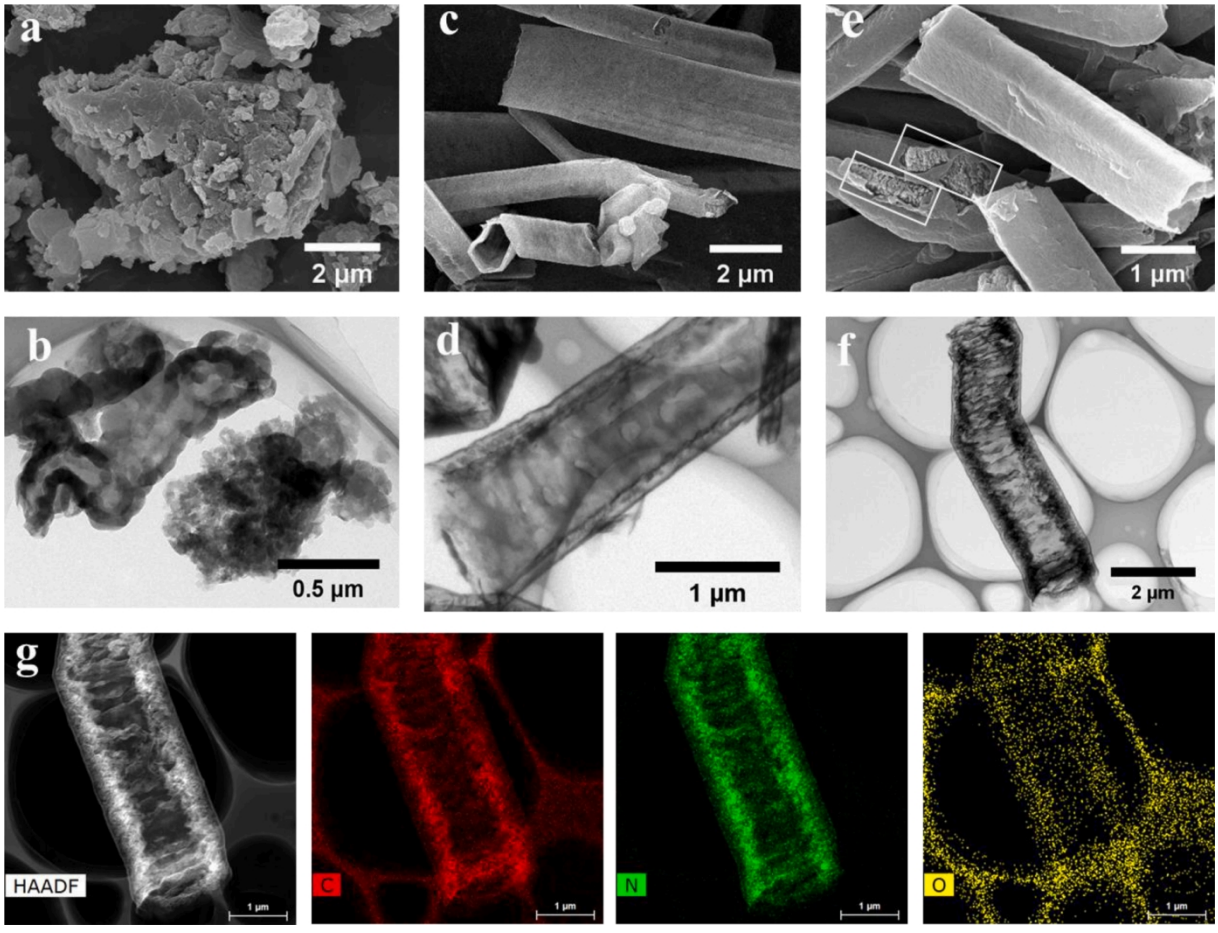

Fig. 1. SEM images of (a) CN, (c) TCN, (e) AN-TCN-4.5 and TEM images of (b) CN, (d) TCN, (f) AN-TCN-4.5; the elemental mapping of AN-TCN-4.5 (g).

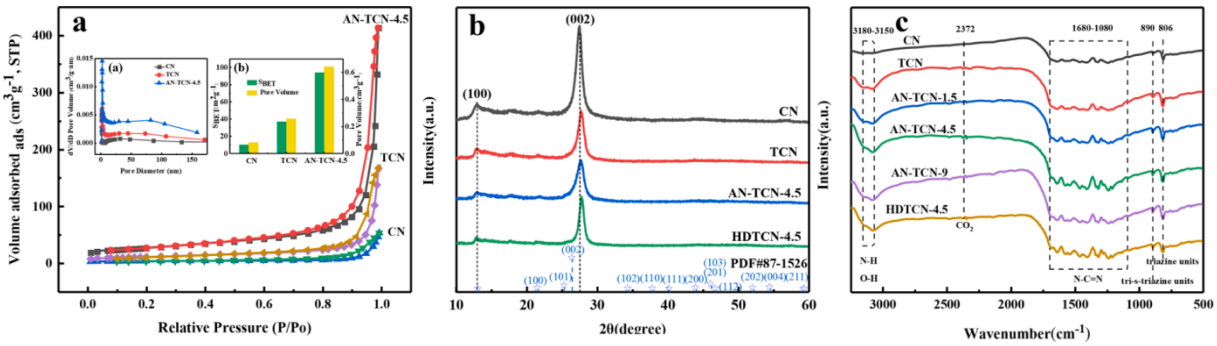

Fig. 2. N_2 adsorption–desorption isotherms, pore size distribution, specific surface area and pore volume (a) of CN, TCN and AN-TCN-4.5; the XRD (b) and FTIR (c) of the CN, TCN, AN-TCN-4.5 and HDTCN-4.5.

indicated that H_2O_2 could destroy the ordered extension of heptazine ring during thermal polymerization but could not destroy the crystal structure of synthesized g-C_3N_4. Meanwhile, it also suggested that supramolecular structures formed by hydrogen bond self-assembly were more susceptible to H_2O_2 molecules, thus leading to the formation of ant nest-like porous structure.

In order to investigate the surface functional groups of the prepared samples, FTIR spectroscopy was performed. Displayed as Fig. 2c, all the samples demonstrated a similar characteristic peak around at 806 cm^{-1}, 1080 ~ 1680 cm^{-1}, and 3150 ~ 3180 cm^{-1}, representing the breathing mode of the triazine units, stretching mode of aromatic C—N heterocycles, and the stretching mode of residual amino group (N—H and N-H_2) and O-—H interactions of absorbed H_2O, respectively [35]. The peak around 887 cm^{-1} was caused by the characteristic bending vibration of the extended conjugated networks with heptazine ring units [36–38]. This indicated that the prepared materials contained a well-defined g-C_3N_4 structure. The absorption strength of AN-TCN samples at 3150–3180 cm^{-1} was greater than that of CN and TCN, indicating that AN-TCN contained more amino groups, which was attributed to the fact that the gas generated by H_2O_2 and H_2O broke through the network structure of g-C_3N_4 during thermal polymerization [39]. Therefore, mesoporous structure was constructed and more reactive sites were exposed, which was benefited to the improvement of catalytic efficiency.

The surface chemical state of the as-synthesized samples was investigated by XPS and the result was firstly corrected through the standard C peak that was 284.8 eV. The survey spectra showed that all the samples were mainly formed by C, N, and O elements (Fig. 3a). The O 1s

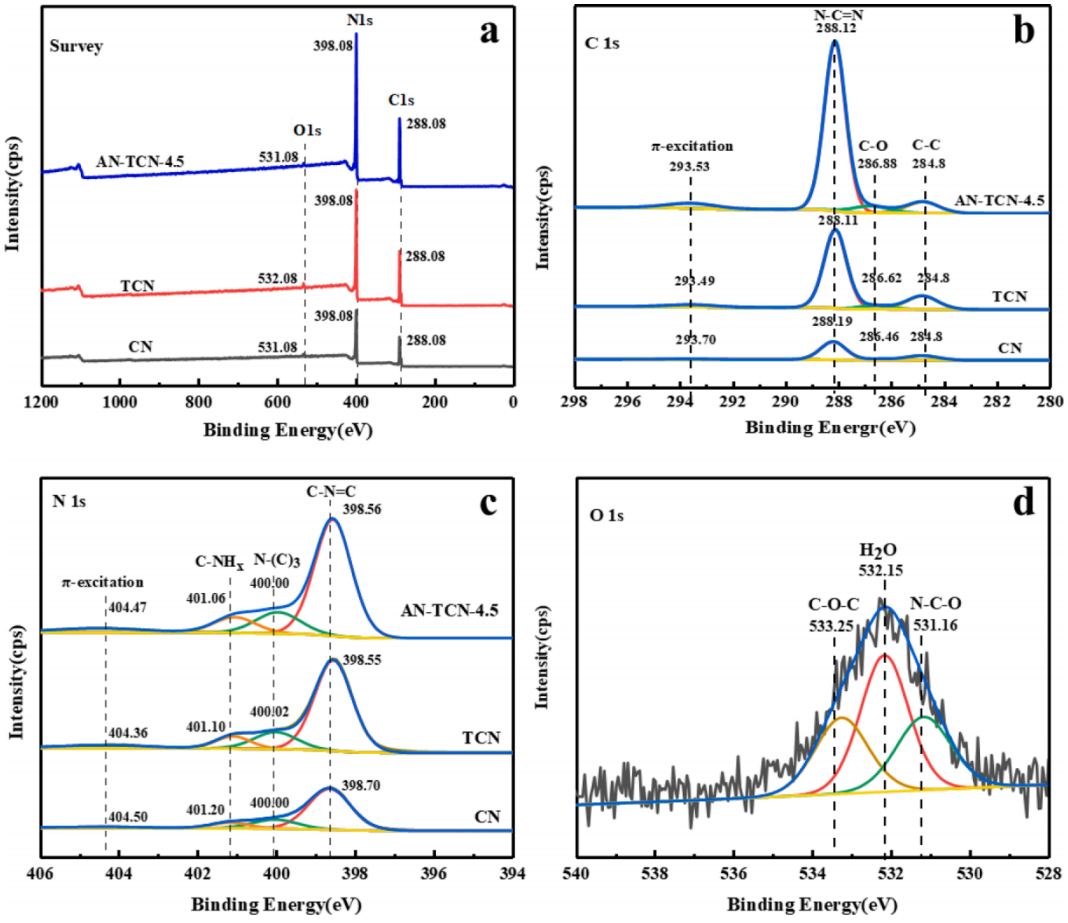

Fig. 3. XPS spectra of CN, TCN and AN-TCN-4.5: survey (a), C 1 s (b), N 1 s (c), O 1 s of AN-TCN-4.5(d).

might come from the absorbed oxygen-containing species such as H_2O and CO_2 molecules [38,40]. Fig. 3b exhibited the high-resolution XPS spectra of C 1s, the peak at 284.8 eV represented the sp^2 hybridized carbon in C—C bonds. The peaks around 288.1 eV and 286.6 eV originated from the C atom in N═C-N heterocycle and C—O bond, respectively. Then the peaks at binging energy of 293.5 eV were corresponded to the π-excitation. In comparison with CN and TCN, the peak area rate of N═C-N in AN-TCN-4.5 was slight decreased, meaning that part of N═C-N bonds were destroyed. Meanwhile, the increased proportion of C—O bonds might derive from the breakdown of the N-C═N heterocycles or bridge N-(C)3 bonds and to generate C—O (Table S1) [41,42]. In order to further understand the structural changes of AN-TCN-4.5, the high-resolution XPS spectra of N 1s was also analyzed. Shown as Fig. 3c, the peaks around 398.6 eV, 400 eV and 401.1 eV corresponded to the sp^2 hybridized nitrogen in the C-N═C, sp^3 hybridized nitrogen in the N-(C)3 and nitrogen atom in C-NH_x groups, respectively. And the peak around 404.4 eV represented π-excitation [38]. The proportions of each group were calculated as Table S2, which showed that the content of N-(C)3 in AN-TCN-4.5 and TCN were comparable, while the ratio of C-N═C in AN-TCN-4.5 was less than that in TCN. This was consistent with the results in Table S1, indicating that the bridged N-(C)3 remained intact while the C-N═C bond of AN-TCN-4.5 was changed. Then in order to further determine the cause of the change of C-N═C bond, the surface chemical state of O1s was also tested. The O 1s peak at 531.16 eV and 533.25 eV were corresponded to the N—C—O and C—O—C bond, respectively [43,44]. And the peak at 532.15 eV corresponded to the absorbed H_2O molecule (Fig. 3d). On the basis of the above XPS results, the oxygen atoms were dopped in the AN-TCN-4.5 by substituting N atoms in C-N═C and connected with sp^2 hybrid carbon atoms was confirmed, which was consistent with previous studies [41,44,45]. Moreover, the larger peak area ratio of C—O/N═C-N in AN-TCN-4.5 in Table S1 also reflected this result. Then the increased proportion of C-NH_x in AN-TCN-4.5 originated from the porous structure of AN-TCN, which would expose more edge N atoms.

According to the results of XPS, DFT was applied to simulate the electronic properties of g-C_3N_4 before and after oxygen doping. A 2 × 2

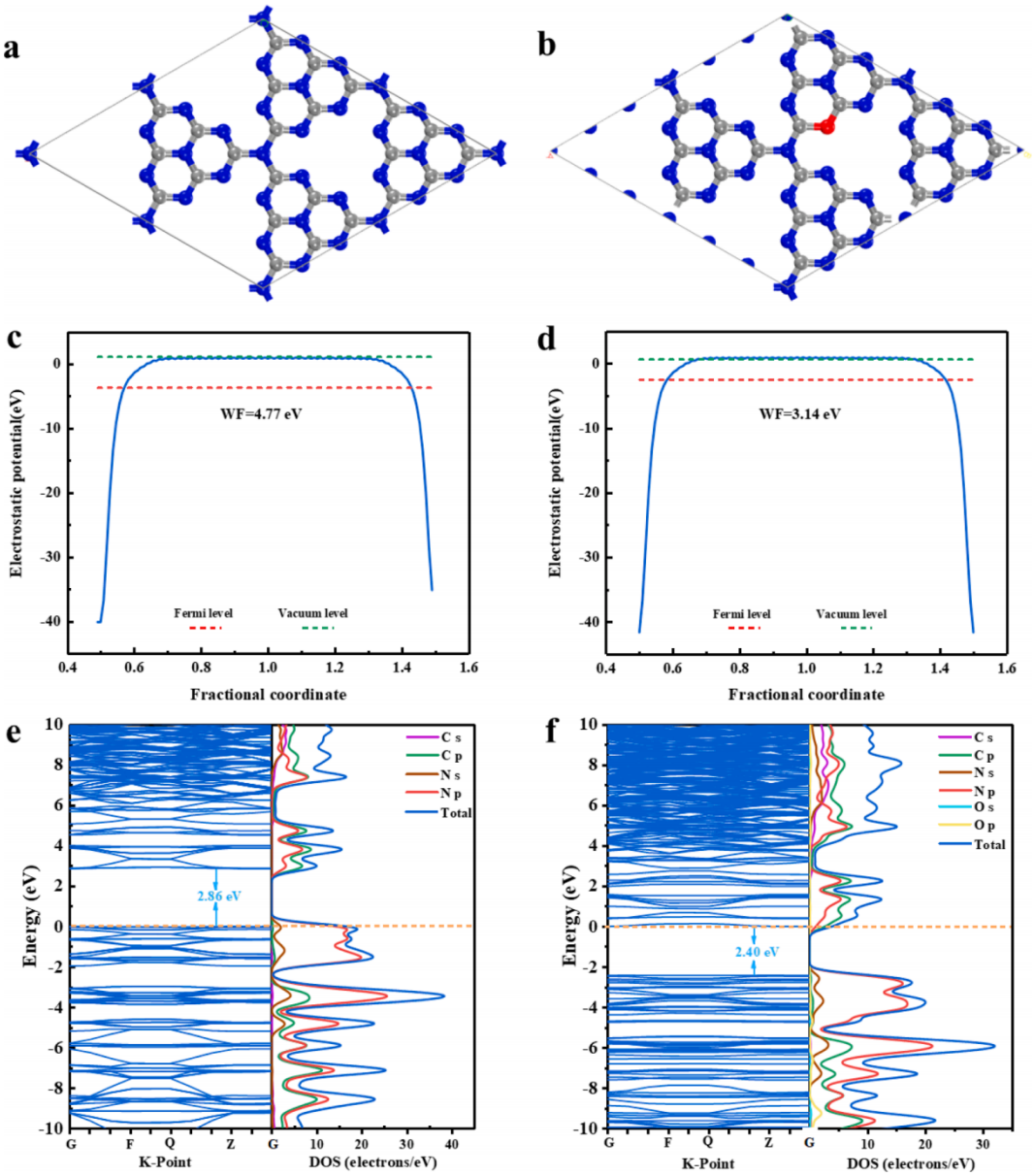

Fig. 4. The calculation models of CN (a) and AN-TCN-4.5 (b) after geometry optimization; the work function of CN (c) and AN-TCN-4.5 (d); the band gap structure and partial density of states (PDOS) of CN (e) and AN-TCN-4.5 (f).

× 1 supercell was used as the simulation model. Fig. 4a-b and Fig. S7a-b showed the structural optimization model of g-C_3N_4 before and after oxygen doping. And Fig. S7c-d showed that the bond length was changed after oxygen doping. Fig. 4c-d indicated that the work functions of CN and AN-TCN were 4.77 eV and 3.14 eV, respectively. The smaller work function of AN-TCN indicating that the binding force of the electron escaping from the potential well to the surface of AN-TCN was reduced, thereby the separation and migration of photogenerated electrons was promoted. The band structure distribution and partial density of states (PDOS) shown as Fig. 4e-f and Fig. S8 indicated that doping of oxygen atom would change the electronic structure of g-C_3N_4. The valence band (VB) of CN and AN-TCN were mainly contributed by N 2p orbital and the conduction band (CB) were composed by both N 2p and C 2p orbital. In addition, O 2p contributed a little to the VB of AN-TCN. In addition, doping of oxygen atom also caused the change of band gap structure. The narrower band gap energy of oxygen-doped AN-TCN (2.40 eV) than that of undoped CN (2.86 eV) enabled a higher visible light utilization. Furthermore, the differential charge densities revealed a charge transfer between the doped oxygen atom and the surrounding atoms (Fig. S9a-b). The electron cloud density of carbon atoms around the doped oxygen atoms was decreased, leading to the generation of a new internal electric field, which benefiting to the transport and separation of photogenerated electrons [46].

3.4. Photoelectric characteristics

The optical property of the prepared samples was measured by UV–vis diffuse reflectance spectrum firstly. Shown as Fig. 5a, the light absorption intensity of AN-TCN in the visible region first increased and then decreased with the increase of H_2O_2 concentration, and AN-TCN-4.5 had the highest visible light absorption capacity among the prepared samples. Besides, the porous bulk PCN exhibited slightly higher absorption capacity of visible light than CN due to its porous structure, and all the prepared AN-TCN samples possessed stronger visible light absorption than the bulk CN and PCN due to their more mesoporous structures, which demonstrated the excellent light utilization performance of AN-TCN. The abundant mesoporous structure in AN-TCN-4.5 and PCN was beneficial to the diffuse reflection of incident light, so that the incident light could be absorbed multiple times and thus to achieve higher light absorption capacity [47]. According to the Kubelka-Munk function (Eq. (1)), the energy gap of the synthesized samples was calculated [48]:

$$\alpha h\nu = A\left(h\nu - E_g\right)^{n/2} \tag{1}$$

α is the absorption coefficient, h represents Planck constant, v corresponds to the frequency of incident light and A is a constant. E_g represents the band gap energy of the synthesized samples. The value of n is be determined by the type of semiconductor, n is 1 for direct bandgap semiconductor and 4 for indirect bandgap semiconductor [49]. Due to g-C_3N_4 is direct bandgap semiconductor, therefore n equal to 1 was selected to calculate the band gap of the synthesized samples [50]. The band gap energy of CN, TCN and AN-TCN-4.5 were calculated to be 2.66 eV, 2.43 eV and 2.48 eV (inset in Fig. 5a), respectively, which were well agreement with the results of DFT calculation. With the increase of the concentration of H_2O_2 solution, the band gap energy of AN-TCN samples increased gradually, indicating that H_2O_2 treatment could indeed change the electronic structure of g-C_3N_4. And the HDTCN-4.5 showed a lower band gap energy than that of CN, TCN and AN-TCN might due to the thinner tube walls after two thermal polymerization treatments [47]. Then PCN and CN had similar band gap widths, which might be due to their bulk structures.

Subsequently, in order to obtain the distribution of energy band structure, the Mott-Schottky curves was carried out to evaluate the CB of prepared samples. The result showed that the flat band potentials of CN, TCN and AN-TCN-4.5 were −0.74 V, −0.74 V and −0.89 V (vs. SCE), respectively, indicating that the synthesized samples were *n*-type semiconductors (Fig. 5b). Then the flat band potentials of CN, TCN and AN-TCN-4.5 were calculated to −0.50 V, −0.50 V and 0.64 V (vs. NHE), respectively, which were approximately equal to their conduction band minimum (E_{CBM}). According to the Eq. (2):

$$E_{VBM} = E_{CBM} + E_g \tag{2}$$

The valence band minimum (E_{VBM}) of CN, TCN and AN-TCN-4.5

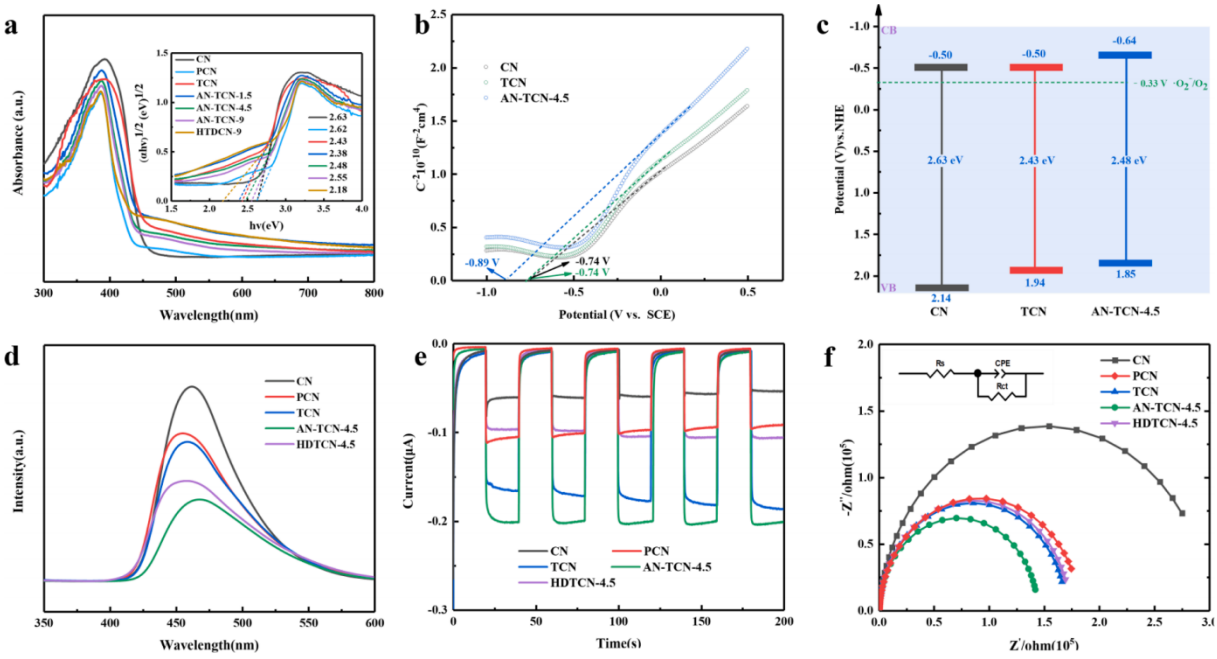

Fig. 5. UV–vis DRS and band gap energy of CN, PCN, TCN, AN-TCN, HDTCN-4.5 (a); the Mott-Schottky curves of CN, TCN, AN-TCN-4.5 (b); Eg and the potential of E_{CBM} and E_{VBM} distribution of CN, TCN, AN-TCN (c); photoluminescence emission spectra (PL) of CN, PCN, TCN, AN-TCN, HDTCN-4.5 (d); photocurrent response spectra of CN, PCN, TCN, AN-TCN, HDTCN-4.5 (e); and Nyquist plots in a three electrodes system with 0.2 M $NaSO_4$ electrolyte of CN, PCN, TCN, AN-TCN, HDTCN-4.5(f).

were calculated to 2.14 V, 1.94 V and 1.85 V (vs. NHE), respectively. Then the Fermi level (E_f) could be speculated according to the difference between E_{VBM} and XPS valence bands ($E_{XPS\text{-}VB}$) (Fig. S6) (Eq. (3)).

$$E_f = E_{VBM} - E_{VB-XPS} \quad (3)$$

That was, the E_f of CN, TCN, AN-TCN-4.5 were matched to 0.38 eV, 0.34 eV, and 0.25 eV, respectively. Subsequently, the work function (Φ) was obtained by Eq. (4):

$$\Phi = E_{vacuum} - E_f \quad (4)$$

Since the potential difference between the vacuum level (E_{vacuum}) and the normal hydrogen electrode is 0.45 eV, the calculated work functions of CN, TCN, AN-TCN-4.5 were 4.88 eV, 4.84 eV and 4.75 eV (vs. NHE), respectively [51], which showed the same trend as the result of DFT calculation, that AN-TCN has a smaller work function. Then the distribution of band structure was displayed as Fig. 5c. The narrow energy band gap of AN-TCN-4.5 enhanced its visible light response ability, meanwhile a more negative conduction band potential was beneficial to generate more superoxide radicals ($\cdot O_2^-$), thereby improving the kinetics of the photocatalytic reaction. In addition, the smaller work function mean that less energy was required for electrons in AN-TCN to move from its interior to the surface, indicating that the photogenerated electrons in AN-TCN-4.5 were more easily migrated, thereby improving the photocatalytic performance. The difference between the DFT calculations and the experimental data might originate from the inability of the used model to distinguish the morphology difference between CN and AN-TCN.

In addition, the PL spectroscopy was performed to measure the recombination efficiency of photogenerated carrier at an excitation wavelength of 320 nm (Fig. 5d). The results showed that the emission intensity of the samples was AN-TCN-4.5 < HDTCN-4.5 < TCN < PCN < CN, indicating that the recombination efficiency of photoinduced electron-hole pairs was AN-TCN-4.5 < HDTCN-4.5 < TCN < PCN < CN. Compared with CN, the photocarrier recombination efficiency of PCN was lower, and AN-TCN-4.5 also displayed the same phenomenon compared with TCN, which proved the important role of porous structure in inhibiting e^--h^+ recombination. Besides, the emission intensity of the porous AN-TCN-4.5 was significantly lower than that of the porous PCN, proving that not only the tubular structure could effectively suppress the recombination of photoinduced carriers, but also the porous ant nest-like filling structure inside AN-TCN-4.5 and oxygen doping would further reduce the recombination of photogenerated carriers. The reasons might be attributed to the following: (1) the tubular structure promoted the directional flow of photogenerated electron while suppressing the recombination of photoinduced electron-hole pairs [34]; (2) the orderly stacked mesoporous-rich ant nest-like filling structure inside AN-TCN-4.5 shortened the distance of electron transfer from the inside of the crystal to the surface [52]; (3) the lone pair electrons of the doped oxygen atom was delocalized to the oxygen-doped aromatic system resulted in an increasing of the charge density and mobility; (4) the change of C—N bond length caused by oxygen doping resulted in a lattice strain and electron polarization effect, which would form an internal electric field favorable to the separation of electron-hole pairs [53].

Furthermore, photochemical tests were further performed to investigate the behavior of photogenerated carriers of the prepared samples. The results show that AN-TCN-4.5 has the higher transient photocurrent response intensity than the unfilled TCN, bulk CN, HTDCN-4.5 and even porous PCN (Fig. 5e), indicating the faster photoinduced charge transfer rate and longer lifetime of AN-TCN-4.5. Meanwhile, the EIS Nyquist plot (Fig. 5f) also showed that AN-TCN-4.5 had the smaller radius compared with CN, PCN, TCN and HDTCN-4.5, meaning that AN-TCN-4.5 has the lower interface resistance, which was favorable for the transfer of photoinduced charges.

The above photochemical test results proved that the multi-mesoporous structure and well-defined band structure of AN-TCN-4.5 promoted its excellent photoelectric performance. At the same time, attributing to the ordered lamellar stacked ant nest-like filling structure and a small amount of oxygen doping, AN-TCN-4.5 had a fast transfer rate and a low recombination efficiency of photogenerated carriers, which further guaranteed its outstanding photocatalytic performance.

3.5. Photocatalysis experiment

The actual photocatalytic capability of the synthesized samples was assessed mainly by degradation of TCH. Three parallel experiments were performed for each group of degradability tests, and the data errors at each time point were shown by error bars. Before irradiation, the adsorption–desorption experiments were carried out in darkness for 0.5 h to reach adsorption equilibrium. The photocatalytic activity for TCH degradation of the prepared samples under visible light irradiations was shown as Fig. 6a. After 30 min of visible light irradiation, 59.1 % of TCH was degraded by CN, which was significantly lower than the degradation efficiency of TCN (76.2 %) and AN-TCN-4.5 (86 %). And the result of TOC showed that AN-TCN-4.5 (55 %) had a higher mineralize ability to TCH than CN (44 %) and TCN (47 %) under visible light irradiation for 30 min (Fig. S10). The photocatalytic efficiency of the AN-TCN samples first increased and then decreased with the increase of the concentration of H_2O_2 used to treat the precursors. This might be due to the too much H_2O_2 would lead to excess pores and defects, which played a role of electron-hole pairs recombination center, thereby inhibiting its photocatalytic efficiency [54]. In addition, the degradation results also showed that TCN, AN-TCN and HDTCN-4.5 with tubular morphology all exhibited higher photocatalytic efficiency than the bulk CN, PCN and HOCN, which again proved the excellent photocatalytic performance of the tubular structure. Moreover, the photodegradation rate constant of different photocatalysts for TCH were achieved by fitting the first-order kinetic equation: $-\ln(C_t/C_0) = kt$. As shown in Fig. 6b, the rate constants of AN-TCN-4.5 were 4.78, 1.26, 1.68 times that of CN, PCN and TCN respectively, indicating that the existence of porous ant nest-like filling structure effectively improved the photocatalytic efficiency of AN-TCN-4.5. To investigate the general applicability of the prepared samples to organic pollutants, the degradation ability of AN-TCN for four other organic pollutants was tested. As shown in Fig. S11, AN-TCN-5 displayed strong adsorption effect on rhodamine B (RhB) and methylene blue (MB), which was benefited from the porous structure of AN-TCN-5. In addition, the opposite electrical properties between pollutants and AN-TCN-4.5 were also another important factor for their efficient adsorption (Table S3 and Table S5). Then the degradation efficiencies of AN-TCN-4.5 for ciprofloxacin (CIP), p-nitrophenol (PNP), RhB and MB reached 55 %, 31 %, 99.6 % and 99.99 % within 1 h, respectively. Although AN-TCN-4.5 showed an unsatisfactory ability to photodegrade CIP and PNP, it had strong photodegradation ability to dyes, which again demonstrated the strong photocatalytic effect of AN-TCN-4.5. In addition, the ability of AN-TCN-4.5 to degrade TCH was compared with other g-C_3N_4-based photocatalysts (Table S4), and the results showed that AN-TCN-4.5 had promising photocatalytic performance.

Subsequently, the degradation capacity of AN-TCN-4.5 under different pollutant concentrations was observed. As shown in Fig. 6c, as the increase of pollutant concentration from 5 mg L^{-1} to 30 mg L^{-1}, the degradation ability of AN-TCN-4.5 to TCH gradually decreased, which ascribing to the increased concentration of pollutants leaded to a relative decrease in the number of reaction active sites under the condition of quantitative catalyst. In addition, the effects of different pH environments and different common anions on the degradation of TCH by AN-TCN-4.5 were also investigated. The results showed that despite the pH did not affect the catalytic performance of AN-TCN-4.5 significantly, the alkaline conditions would inhibit the final degradation effect (Fig. 6d), which was due to the fact that the surface of AN-TCN-4.5 was negatively charged under alkaline conditions (Table S5), while the tetracycline molecules gradually became neutral or negative charge

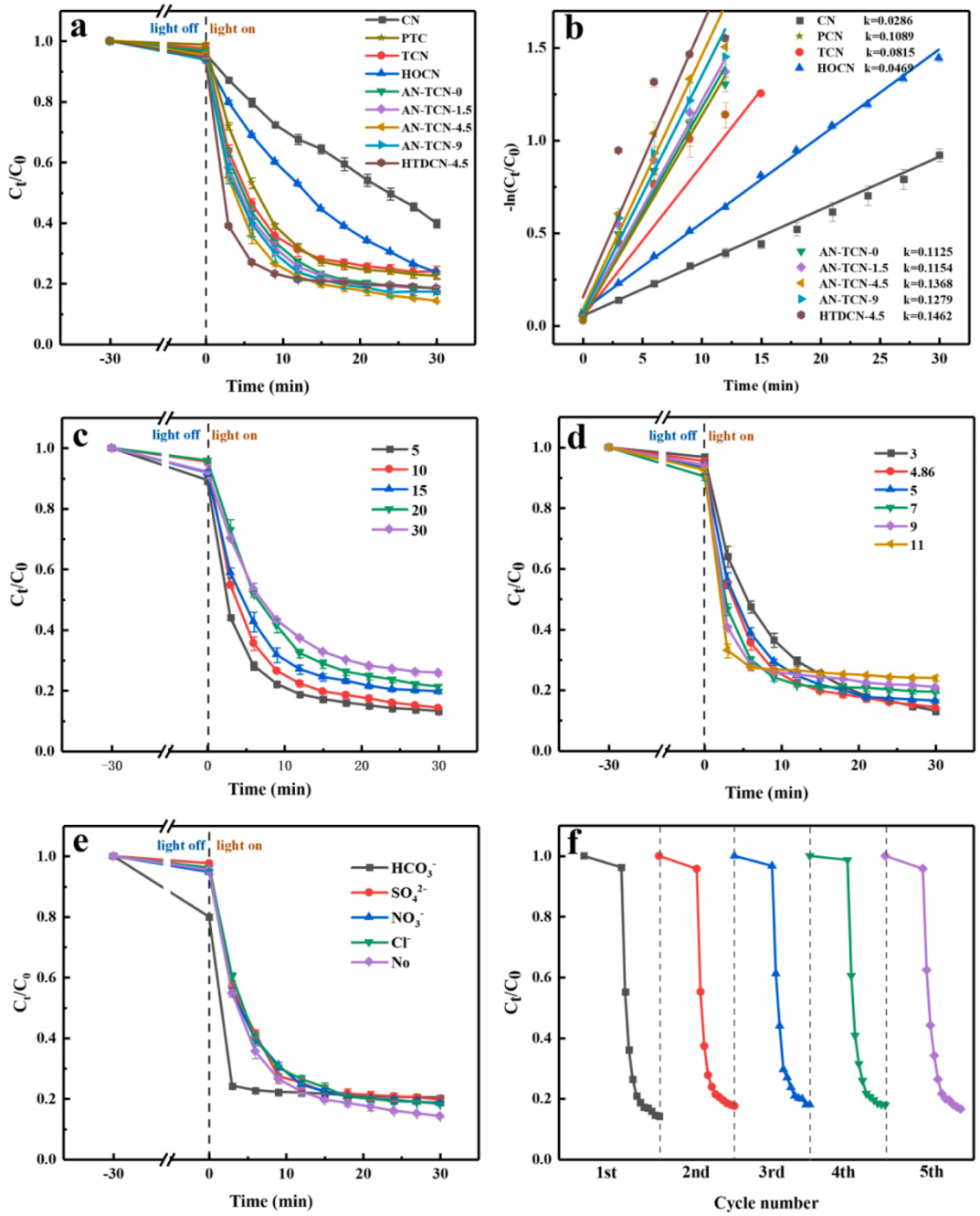

Fig. 6. TCH degradation rates by using CN, PCN, TCN, AN-TCN, HOCN and HDTCN-4.5 (a); the reaction rate constant of TCH degradation by using CN, TCN, PCN, AN-TCN, HOCN and HDTCN-4.5 (b); the effect of different concentrations of TCH (c), solution pH (d) and anionic electrolyte (e) on photocatalytic degradation of TCH by using AN-TCN-4.5; the reusing experiments of photocatalytic degradation of TCH over AN-TCN-4.5 (f).

through deprotonation, resulting in electrostatic repulsion between the photocatalyst and the pollutant, which ultimately affected its photocatalytic efficiency [55]. Then Fig. 6e showed that HCO_3^-, SO_4^{2-}, NO_3^- and Cl^- ions all had no obvious effect on the photocatalytic performance of AN-TCN-4.5. However, in the presence of HCO_3^-, the photocatalytic reaction exhibited an increased reaction rate in the first 3 min and then reached equilibrium. This may be due to that HCO_3^- increased the pH of the reaction system, making the degradation reaction similar to that in the alkaline environment shown as Fig. 6d. In addition, HCO_3^- could react with hole to generate $HCO_3^{\cdot}$ (Eq. (5)), which would promote the separation of electron-hole pairs and ensure the continuous progress of the catalytic reaction through $HCO_3^{\cdot}$ at the same time.

$$HCO_3^- + h^+ \rightarrow HCO_3^{\cdot} \quad (5)$$

Nevertheless, due to the rapid depletion of holes and the low oxidation ability of $HCO_3^{\cdot}$, it was difficult for the pollutant intermediates generated in the early stage to be further degraded, resulting in the obvious inhibition of the reaction efficiency in the later stage [56].

The lifetime of the photocatalyst was always reduced due to its weak resistance to the reaction environment and photocorrosion. To understand the stability of AN-TCN-4.5, five cycle reusing experiments were performed. Fig. 6f showed that the degradation efficiency of AN-TCN-4.5 was still not significantly reduced after five rounds reused, indicating the high photocatalytic stability of AN-TCN-4.5. Then, the structure change of the recycled sample was characterized by XRD and SEM, and it was found that the recycled AN-TCN-4.5 still showed two characteristic peaks of g-C_3N_4, and the peak intensity of the (002)

crystal plane was increased (Fig. S12a), which might be due to the mechanical stirring destroyed the outer tube wall of AN-TCN-4.5 and exposed its inner stacked lamellar ant nest-like filling structure (Fig. S12b). The exposed filling structure with thicker thickness enhanced the diffraction peak intensity of the (002) crystal plane.

3.6. Photocatalytic mechanism

In order to investigate the photocatalytic mechanism for TCH degradation, free radical quenching experiment was implemented to investigate the active species present during the process of TCH degradation. In detail, 10 mM 4-hydroxy-2,2,6,6-tetramethylpiperidine-*N*-oxyl (TEMPOL), ethylenediamine tetraacetic acid disodium (EDTA-2Na) and isopropyl alcohol (IPA) were applied for quenching $\cdot O_2^-$, h^+ and ·OH, respectively. Fig. 7a showed that the existence of IPA had almost no influence on the degradation efficiency of TCH, while after the introduction of TEMPOL and EDTA-2Na, the degradation efficiency was reduced to 19 % and 66 %, which indicated that the main active species for TCH degradation were $\cdot O_2^-$ and h^+ were. This result was related to the band gap structure of AN-TCN-4.5, namely, the CB potential of AN-TCN-4.5 was more negative than the potential of generating $\cdot O_2^-$ (-0.33 V), while the potential of the VB was lower than the potential of generating ·OH (+1.99 V). Therefore the $\cdot O_2^-$ could be generate but not ·OH by AN-TCN-4.5, and the main active species were $\cdot O_2^-$ and h^+ could be concluded. Subsequently, the contribution ratios of these active species were analyzed according to the Eqs. (6)-(7) [57]:

$$\ln\left(\frac{C_t}{C_0}\right) = -K_{app}t \tag{6}$$

$$R_I = \frac{K_I}{K_{app}} \approx \frac{K_{app} - K_i}{K_{app}} \tag{7}$$

K_{app} represents the apparent rate constant for TCH degradation, which is calculated from the quasi-first-order kinetic model; K_I (I represents $\cdot O_2^-$, h^+ or $\cdot OH^-$) corresponds to the rate constant for the photocatalytic degradation of TCH in the existence of $\cdot O_2^-$, h^+, and ·OH, respectively; K_i (i represents TEMPOL, EDTA-2Na or IPA) is the rate constants of the photodegradation of TCH in the existence of the corresponding radical scavenger (Fig. 7b). R_I represents the contribution rate of I active species. The quencher i (TEMPOL, EDTA-2Na, IPA) is corresponding to the I active specie ($\cdot O_2^-$, ·OH, h^+). As shown in Fig. 7c, the rate constants were 0.0049, 0.0326 and 0.1013 min^{-1} respectively when TEMPOL, EDTA-2Na and IPA were present during the degradation process. According to the Eq. (7), the contribution rate of $\cdot O_2^-$, h^+ and ·OH were 96.11 %, 74.14 % and 19.70 %, respectively. The above results indicated that both $\cdot O_2^-$ and h^+ played a crucial part in the degradation of TCH. It is worth noting that, the total contribution over 100 % might be ascribed to the complex chemical reaction of active species involved in photocatalytic process [57].

In addition, the ESR experiments were also further carried out to investigate the existence of free radicals. The ESR signal of DMPO-$\cdot O_2^-$ and DMPO-·OH were tested under irradiation and non-irradiation conditions. The results showed that the ESR spectrum of DMPO-$\cdot O_2^-$ appeared four strong signals with an intensity ratio of about 1:1:1:1, and

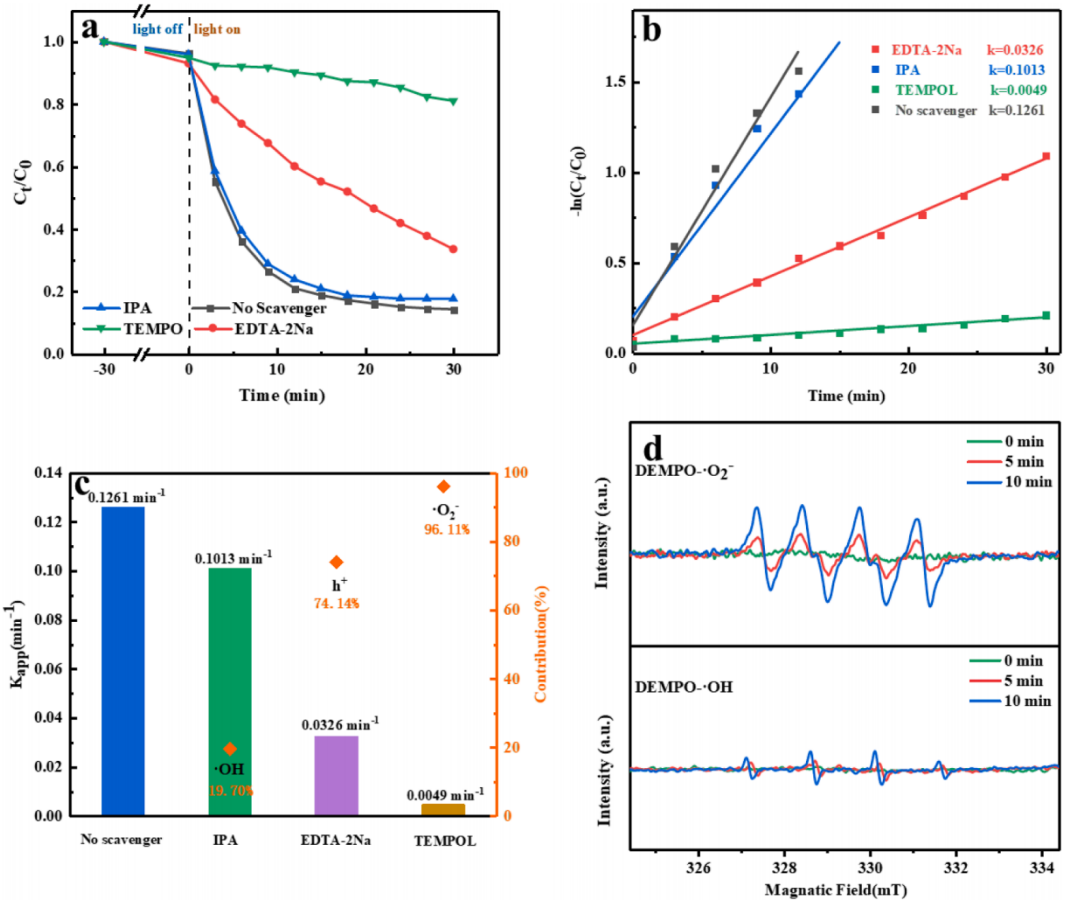

Fig. 7. Radicals ($\cdot O_2^-$, h^+ and ·OH) capture experiment of photocatalytic degradation of TCH by using 10 mM TEMPOL, EDTA-2Na and IPA (a); the rate constants for photocatalytic degradation of TCH in the presence of different trapping agents (b); the rate constants (columns, primary y-axis) and percent contribution of different radicals (points, secondary y-axis) for TCH degradation (c); the ESR signals of DMPO-$\cdot O_2^-$ and DMPO-·OH under visible light irradiation on 0 min, 5 min and 10 min (d).

the signal strength was enhanced with the increase of light irradiation time, indicating that $\cdot O_2^-$ was generated under visible light irradiation. Besides, the ESR spectra of DMPO-·OH displayed four signal peaks with a strength ratio of 1:2:2:1, and the peak intensity also enhanced with the prolonging of radiation time, which indicated that ·OH was also produced by AN-TCN-4.5. However, the peak intensity of DMPO-·OH was significantly lower than that of DMPO-$\cdot O_2^-$, indicating that more $\cdot O_2^-$ than ·OH was produced in this reaction system, which was consistent with the results of radical trapping experiments (Fig. 7d). This result again proved the important role of $\cdot O_2^-$ in TCH degradation by AN-TCN-4.5. In addition, the stability of AN-TCN-4.5 was maintained due to the absence of ·OH, which was the main active substance that destroyed g-C_3N_4 [58].

Subsequently, in order to explore the degradation products and degradation paths of TCH, high-performance liquid-mass spectrometry (HPLC-MS) was applied to identify intermediates during the degradation process. According to Fig. S13a, there was a strong signal peak at the mass-to-charge ratio (*m/z*) of 445, corresponding to TC molecule. After 10 ~ 30 min of degradation, the signal peak intensity of TC decreased rapidly, and multiple new signal peaks were generated (Fig. S13b-d). The intermediate with *m/z* of 431 was produced by *N*-demethylation of TC molecule [11], and followed produced the product with *m/z* of 358 through a series of demethylation and deamination processes. Then the intermediate product with *m/z* of 272 was produced by ring-opening [59]. Besides, the intermediate product with *m/z* of 460 was produced by hydroxylation of TC molecule. Further hydroxylation would yield an intermediate with m/s of 459, followed by dealkylation, deamination and ring opening to give an intermediate with m/s of 343 [60]. Then these intermediates would continue to undergo a series of mineralization to generate CO_2 and H_2O according to the result of TOC test, that the mineralization rate of TCH was 55 % by AN-TCN-4.5 within 30 min (Fig. S10). And the possible degradation pathway was displayed as Fig. 8a.

According to the distribution of band gap structure of AN-TCN-4.5 and the results of free radical investigation, the photocatalytic mechanism of TCH degradation could be inferred as Fig. 8b and Eqs. (8)-(11):

$$AN - TCN + light \rightarrow e^- + h^+ \quad (8)$$

$$O_2 + e^- \rightarrow \cdot O_2^- \quad (9)$$

$$\cdot O_2^- + TCH \rightarrow CO_2 + H_2O \quad (10)$$

$$h^+ + TCH \rightarrow CO_2 + H_2O \quad (11)$$

Firstly, the photogenerated electrons (e^-) were excited and transferred to the CB of AN-TCN-4.5 under light irradiation, while leaving the hole (h^+) in the VB. Subsequently, the electrons arrived at CB reacted with O_2 to generate $\cdot O_2^-$, which degraded TCH simultaneously with h^+. The mesoporous-rich character of AN-TCN-4.5 increased the absorption of visible light radiation and provided a mass of reactive sites for TCH degradation. At the same time, the porous ant nest-like filling structure promoted the generation of more photogenerated charges and facilitated the transfer of photogenerated electrons, thus providing favorable conditions for the high photocatalytic performance of AN-TCN-4.5.

4. Conclusion

In summary, we have successfully synthesized the multi-mesoporous ant nest-like filled tubular g-C_3N_4 with non-hollow structure by supramolecular precursor impregnation method. The decomposition of H_2O_2 and escape of gas molecules during thermal polymerization prompted the formation of mesoporous-rich ant nest-like filling structures, which not only ensured the complete exterior tubular structure of the prepared sample, but also made up for the shortcoming of the hollow part of the hollow tubular g-C_3N_4 being underutilized, so that the entire tubular structure can be fully utilized. The large number of reactive sites, strong visible light absorption properties, and fast separation and transport of photoinduced carriers contributed to the excellent photocatalytic

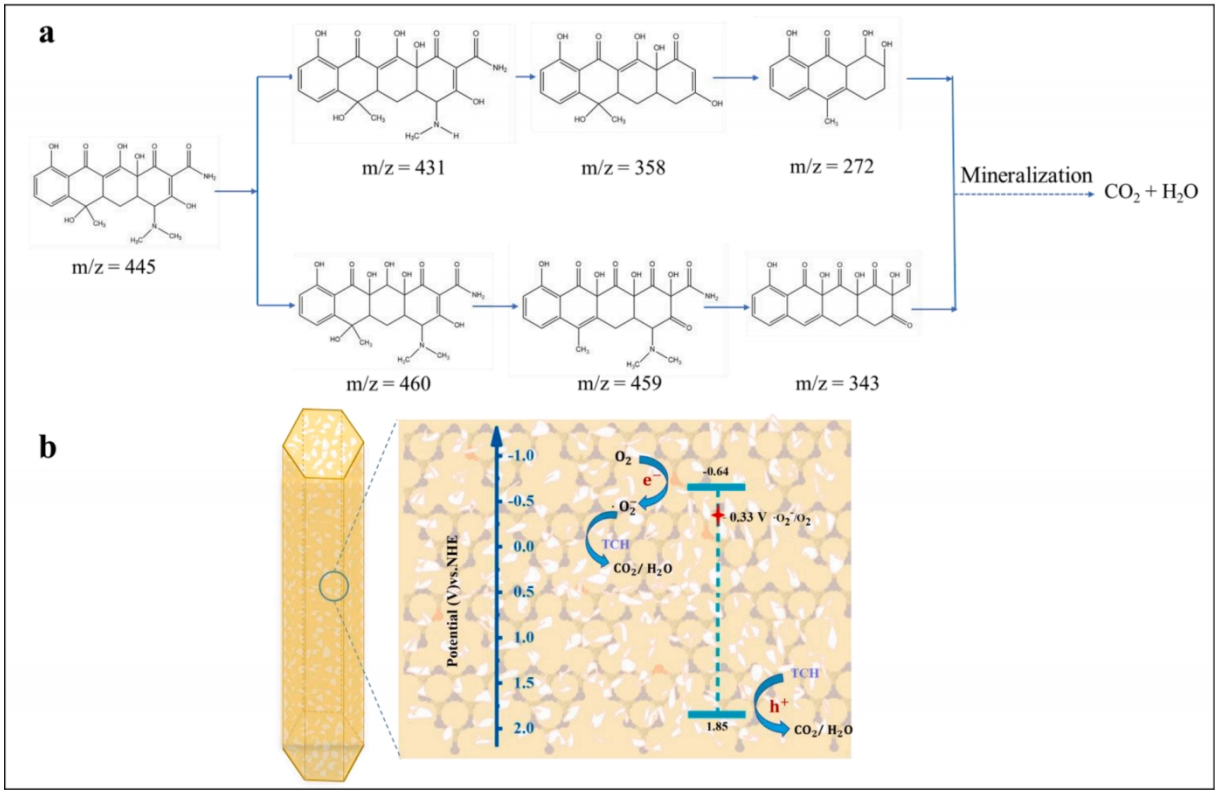

Fig. 8. (a) The possible degradation pathway of TCH inferred from HPLC-MS results; (b) the speculated mechanism of photocatalytic degradation of TCH by AN-TCN-4.5.

property of AN-TCN-4.5. A small number of doped oxygen atoms also provided a favorable condition for photogenerated electron transfer. Under 30 min of light irradiation, the photocatalytic degradation efficiency of TCH of AN-TCN-4.5 reached to 86 %, which was 12 % higher than that of hollow TCN and 24 % higher than that of bulk CN. Besides, the prepared AN-TCN-4.5 maintained excellent photocatalytic stability in an oxidizing environment and wide pH range. This work provided new enlightenment and reference for improving the physicochemical property of photocatalyst by morphology tuning.

Declaration of Competing Interest

The authors declare that they have no known competing financial interests or personal relationships that could have appeared to influence the work reported in this paper.

Acknowledgements

The study was financially supported by the Program for Changjiang Scholars and Innovative Research Team in University (IRT-13R17), the Natural Science Foundation of China (51979103, 51909085, 51579096, 51521006, 51508177), the Funds of Hunan Science and Technology Innovation Project (2018RS3115, 2020RC5012), the Key Research and Development Project of Hunan Province of China (2017SK2241), the Project funded by China Postdoctoral Science Foundation (2021T140192, 2021M690054). The authors also gratefully acknowledge the High-performance Computing Center in Guangxi University for providing the computing resources.

Appendix A. Supplementary data

Supplementary data to this article can be found online at https://doi.org/10.1016/j.cej.2022.137332.

References

[1] T. Wu, X. Liu, Y. Liu, M. Cheng, Z. Liu, G. Zeng, B. Shao, Q. Liang, W. Zhang, Q. He, W. Zhang, Application of QD-MOF composites for photocatalysis: energy production and environmental remediation, Coord. Chem. Rev. 403 (2020), 213097, https://doi.org/10.1016/j.ccr.2019.213097.

[2] Y. Pan, X. Liu, W. Zhang, Z. Liu, G. Zeng, B. Shao, Q. Liang, Q. He, X. Yuan, D. Huang, M. Chen, Advances in photocatalysis based on fullerene C60 and its derivatives: properties, mechanism, synthesis, and applications, Appl. Catal. B-Environ. 265 (2020), 118579, https://doi.org/10.1016/j.apcatb.2019.118579.

[3] W. Zhang, Z. Zeng, Z. Liu, J. Huang, R. Xiao, B. Shao, Y. Liu, Y. Liu, W. Tang, G. Zeng, J. Gong, Q. He, Effects of carbon nanotubes on biodegradation of pollutants: positive or negative? Ecotoxicol. Environ. Saf. 189 (2020), 109914 https://doi.org/10.1016/j.ecoenv.2019.109914.

[4] Q. He, P. Xu, C. Zhang, G. Zeng, Z. Liu, D. Wang, W. Tang, H. Dong, X. Tan, A. Duan, Influence of surfactants on anaerobic digestion of waste activated sludge: acid and methane production and pollution removal, Crit. Rev. Biotechnol. 39 (5) (2019) 746–757, https://doi.org/10.1080/07388551.2018.1530635.

[5] B. Shao, Z. Liu, G. Zeng, Y. Liu, Q. Liang, Q. He, T. Wu, Y. Pan, J. Huang, Z. Peng, S. Luo, C. Liang, X. Liu, S. Tong, J. Liang, Synthesis of 2D/2D CoAl-LDHs/Ti3C2Tx Schottky-junction with enhanced interfacial charge transfer and visible-light photocatalytic performance, Appl. Catal. B-Environ. 286 (2021), 119867, https://doi.org/10.1016/j.apcatb.2020.119867.

[6] Z. Peng, X. Liu, W. Zhang, Z. Zeng, Z. Liu, C. Zhang, Y. Liu, B. Shao, Q. Liang, W. Tang, X. Yuan, Advances in the application, toxicity and degradation of carbon nanomaterials in environment: A review, Environ Int 134 (2020), 105298, https://doi.org/10.1016/j.envint.2019.105298.

[7] S. Xiao, M. Cheng, H. Zhong, Z. Liu, Y. Liu, X. Yang, Q. Liang, Iron-mediated activation of persulfate and peroxymonosulfate in both homogeneous and heterogeneous ways: a review, Chem. Eng. J. 384 (2020), 123265, https://doi.org/10.1016/j.cej.2019.123265.

[8] P. Melchiorre, Introduction: photochemical catalytic processes, Chem. Rev. 122 (2) (2022) 1483–1484, https://doi.org/10.1021/acs.chemrev.1c00993.

[9] D. Zhao, C.L. Dong, B. Wang, C. Chen, Y.C. Huang, Z. Diao, S. Li, L. Guo, S. Shen, Synergy of dopants and defects in graphitic carbon nitride with exceptionally modulated band structures for efficient photocatalytic oxygen evolution, Adv. Mater. 31 (43) (2019) e1903545.

[10] X. Wang, K. Maeda, A. Thomas, K. Takanabe, G. Xin, J.M. Carlsson, K. Domen, M. Antonietti, A metal-free polymeric photocatalyst for hydrogen production from water under visible light, Nat Mater 8 (1) (2009) 76–80, https://doi.org/10.1038/nmat2317.

[11] Q. Liang, X. Liu, J. Wang, Y. Liu, Z. Liu, L. Tang, B. Shao, W. Zhang, S. Gong, M. Cheng, Q. He, C. Feng, In-situ self-assembly construction of hollow tubular g-C3N4 isotype heterojunction for enhanced visible-light photocatalysis: experiments and theories, J. Hazard. Mater. 401 (2020), 123355, https://doi.org/10.1016/j.jhazmat.2020.123355.

[12] Z. Liu, Y. Jiang, X. Liu, G. Zeng, B. Shao, Y. Liu, Y. Liu, W. Zhang, W. Zhang, M. Yan, X. He, Silver chromate modified sulfur doped graphitic carbon nitride microrod composites with enhanced visible-light photoactivity towards organic pollutants degradation, Compos. Pt. B-Eng. 173 (2019), 106918, https://doi.org/10.1016/j.compositesb.2019.106918.

[13] S. Luo, Z. Zeng, G. Zeng, Z. Liu, R. Xiao, P. Xu, H. Wang, D. Huang, Y. Liu, B. Shao, Q. Liang, D. Wang, Q. He, L. Qin, Y. Fu, Recent advances in conjugated microporous polymers for photocatalysis: designs, applications, and prospects, J. Mater. Chem. A 8 (14) (2020) 6434–6470, https://doi.org/10.1039/d0ta01102a.

[14] J. Yuan, X. Liu, Y. Tang, Y. Zeng, L. Wang, S. Zhang, T. Cai, Y. Liu, S. Luo, Y. Pei, C. Liu, Positioning cyanamide defects in g-C3N4: Engineering energy levels and active sites for superior photocatalytic hydrogen evolution, Appl. Catal. B-Environ. 237 (2018) 24–31, https://doi.org/10.1016/j.apcatb.2018.05.064.

[15] B. Shao, J. Wang, Z. Liu, G. Zeng, L. Tang, Q. Liang, Q. He, T. Wu, Y. Liu, X. Yuan, Ti3C2Tx MXene decorated black phosphorus nanosheets with improved visible-light photocatalytic activity: experimental and theoretical studies, J. Mater. Chem. A 8 (10) (2020) 5171–5185, https://doi.org/10.1039/c9ta13610j.

[16] B. Shao, Z. Liu, G. Zeng, H. Wang, Q. Liang, Q. He, M. Cheng, C. Zhou, L. Jiang, B. Song, Two-dimensional transition metal carbide and nitride (MXene) derived quantum dots (QDs): synthesis, properties, applications and prospects, J. Mater. Chem. A 8 (16) (2020) 7508–7535, https://doi.org/10.1039/d0ta01552k.

[17] Y. Zhao, Y. Liu, Z. Wang, Y. Ma, Y. Zhou, X. Shi, Q. Wu, X. Wang, M. Shao, H. Huang, Y. Liu, Z. Kang, Carbon nitride assisted 2D conductive metal-organic frameworks composite photocatalyst for efficient visible light-driven H2O2 production, Appl. Catal. B-Environ. 289 (2021), 120035, https://doi.org/10.1016/j.apcatb.2021.120035.

[18] F. He, B. Zhu, B. Cheng, J. Yu, W. Ho, W. Macyk, 2D/2D/0D TiO2/C3N4/Ti3C2 MXene composite S-scheme photocatalyst with enhanced CO2 reduction activity, Appl. Catal. B-Environ. 272 (2020), 119006, https://doi.org/10.1016/j.apcatb.2020.119006.

[19] M.M. Sabzehmeidani, H. Karimi, M. Ghaedi, Nanofibers based quaternary CeO2/Co3O4/Ag/Ag3PO4 S-scheme heterojunction photocatalyst with enhanced degradation of organic dyes, Mater. Res. Bull. 147 (2022), 111629, https://doi.org/10.1016/j.materresbull.2021.111629.

[20] H. Feng, S. Zhang, X. Zhang, B. Liu, N. Tang, Highly efficient visible-light-induced photoactivity of the CdS–Mn/MoS2/CdTe/TiO2 quaternary photocatalyst for label-free immunoassay of tris-(2,3-dibromopropyl) isocyanurate and enhanced solar hydrogen generation, Anal. Methods 10 (28) (2018) 3462–3469, https://doi.org/10.1039/c8ay01050a.

[21] L. Zhou, J. Lei, F. Wang, L. Wang, M.R. Hoffmann, Y. Liu, S.-I. In, J. Zhang, Carbon nitride nanotubes with in situ grafted hydroxyl groups for highly efficient spontaneous H2O2 production, Appl. Catal. B-Environ. 288 (2021), 119993, https://doi.org/10.1016/j.apcatb.2021.119993.

[22] L. Jiang, J. Li, K. Wang, G. Zhang, Y. Li, X. Wu, Low boiling point solvent mediated strategy to synthesize functionalized monolayer carbon nitride for superior photocatalytic hydrogen evolution, Appl. Catal. B-Environ. 260 (2020), 118181, https://doi.org/10.1016/j.apcatb.2019.118181.

[23] Y.S. Jun, J. Park, S.U. Lee, A. Thomas, W.H. Hong, G.D. Stucky, Three-dimensional macroscopic assemblies of low-dimensional carbon nitrides for enhanced hydrogen evolution, Angew. Chem.-Int. Edit. 52 (42) (2013) 11083–11087, https://doi.org/10.1002/anie.201304034.

[24] G. Li, Z. Lian, W. Wang, D. Zhang, H. Li, Nanotube-confinement induced size-controllable g-C3N4 quantum dots modified single-crystalline TiO2 nanotube arrays for stable synergetic photoelectrocatalysis, Nano Energy 19 (2016) 446–454, https://doi.org/10.1016/j.nanoen.2015.10.011.

[25] B. Li, Q. Fang, Y. Si, T. Huang, W.-Q. Huang, W. Hu, A. Pan, X. Fan, G.-F. Huang, Ultra-thin tubular graphitic carbon Nitride-Carbon Dot lateral heterostructures: one-step synthesis and highly efficient catalytic hydrogen generation, Chem. Eng. J. 397 (2020), 125470, https://doi.org/10.1016/j.cej.2020.125470.

[26] Y. Wang, L. Li, Y. Wei, J. Xue, H. Chen, L. Ding, J. Caro, H. Wang, Water transport with ultralow friction through partially exfoliated g-C3 N4 nanosheet membranes with self-supporting spacers, Angew. Chem.-Int. Edit. 56 (31) (2017) 8974–8980, https://doi.org/10.1002/anie.201701288.

[27] E. Mari, P.-C. Tsai, M. Eswaran, V.K. Ponnusamy, Efficient electro-catalytic oxidation of ethylene glycol using flower-like graphitic carbon nitride/iron oxide/palladium nanocomposite for fuel cell application, Fuel 280 (2020), 118646, https://doi.org/10.1016/j.fuel.2020.118646.

[28] X. Zhao, Y. Zhang, X. Zhao, X. Wang, Y. Zhao, H. Tan, H. Zhu, W. Ho, H. Sun, Y. Li, Urea and melamine formaldehyde resin-derived tubular g-C3N4 with highly efficient photocatalytic performance, ACS Appl. Mater. Interfaces 11 (31) (2019) 27934–27943, https://doi.org/10.1021/acsami.9b08483.

[29] Z. Jiang, X. Zhang, H.S. Chen, X. Hu, P. Yang, Formation of g-C3N4 nanotubes towards superior photocatalysis performance, ChemCatChem 11 (18) (2019) 4558–4567, https://doi.org/10.1002/cctc.201901038.

[30] Y. Guo, Q. Liu, Z. Li, Z. Zhang, X. Fang, Enhanced photocatalytic hydrogen evolution performance of mesoporous graphitic carbon nitride co-doped with potassium and iodine, Appl. Catal. B-Environ. 221 (2018) 362–370, https://doi.org/10.1016/j.apcatb.2017.08.075.

[31] S. Guo, Z. Deng, M. Li, B. Jiang, C. Tian, Q. Pan, H. Fu, Phosphorus-doped carbon nitride tubes with a layered micro-nanostructure for enhanced visible-light

photocatalytic hydrogen evolution, Angew. Chem.-Int. Edit. 55 (5) (2016) 1830–1834, https://doi.org/10.1002/anie.201508505.
[32] F. Hou, Y. Li, Y. Gao, S. Hu, B. Wu, H. Bao, H. Wang, B. Jiang, Non-metal boron modified carbon nitride tube with enhanced visible light-driven photocatalytic performance, Mater. Res. Bull. 110 (2019) 18–23, https://doi.org/10.1016/j.materresbull.2018.10.009.
[33] W. Wang, Q. Niu, G. Zeng, C. Zhang, D. Huang, B. Shao, C. Zhou, Y. Yang, Y. Liu, H. Guo, W. Xiong, L. Lei, S. Liu, H. Yi, S. Chen, X. Tang, 1D porous tubular g-C3N4 capture black phosphorus quantum dots as 1D/0D metal-free photocatalysts for oxytetracycline hydrochloride degradation and hexavalent chromium reduction, Appl. Catal. B-Environ. 273 (2020), 119051, https://doi.org/10.1016/j.apcatb.2020.119051.
[34] T. Wu, Q. He, Z. Liu, B. Shao, Q. Liang, Y. Pan, J. Huang, Z. Peng, Y. Liu, C. Zhao, X. Yuan, L. Tang, S. Gong, Tube wall delamination engineering induces photogenerated carrier separation to achieve photocatalytic performance improvement of tubular g-C3N4, J. Hazard. Mater. 424 (2021), 127177, https://doi.org/10.1016/j.jhazmat.2021.127177.
[35] Y. Zhao, Y. Liu, J. Cao, H. Wang, M. Shao, H. Huang, Y. Liu, Z. Kang, Efficient production of H2O2 via two-channel pathway over ZIF-8/C3N4 composite photocatalyst without any sacrificial agent, Appl. Catal. B-Environ. 278 (2020), 119289, https://doi.org/10.1016/j.apcatb.2020.119289.
[36] W. Zheng, N.-B. Wong, W. Wang, G.e. Zhou, A. Tian, Theoretical study of 1,3,4,6,7,9,9b-heptaazaphenalene and its ten derivatives, J. Phys. Chem. A 108 (1) (2004) 97–106.
[37] L. Tian, J. Li, F. Liang, J. Wang, S. Li, H. Zhang, S. Zhang, Molten salt synthesis of tetragonal carbon nitride hollow tubes and their application for removal of pollutants from wastewater, Appl. Catal. B-Environ. 225 (2018) 307–313, https://doi.org/10.1016/j.apcatb.2017.11.082.
[38] J. Yang, Y. Liang, K. Li, G. Yang, K. Wang, R. Xu, X. Xie, One-step synthesis of novel K+ and cyano groups decorated triazine-/heptazine-based g-C3N4 tubular homojunctions for boosting photocatalytic H2 evolution, Appl. Catal. B-Environ. 262 (2020), 118252, https://doi.org/10.1016/j.apcatb.2019.118252.
[39] S. Gao, X. Wang, C. Song, S. Zhou, F. Yang, Y. Kong, Engineering carbon-defects on ultrathin g-C3N4 allows one-pot output and dramatically boosts photoredox catalytic activity, Appl. Catal. B-Environ. 295 (2021), 120272, https://doi.org/10.1016/j.apcatb.2021.120272.
[40] X. Yang, F. Qian, G. Zou, M. Li, J. Lu, Y. Li, M. Bao, Facile fabrication of acidified g-C3N4/g-C3N4 hybrids with enhanced photocatalysis performance under visible light irradiation, Appl. Catal. B-Environ. 193 (2016) 22–35, https://doi.org/10.1016/j.apcatb.2016.03.060.
[41] Y. Gao, Y. Zhu, L. Lyu, Q. Zeng, X. Xing, C. Hu, Electronic structure modulation of graphitic carbon nitride by oxygen doping for enhanced catalytic degradation of organic pollutants through peroxymonosulfate activation, Environ. Sci. Technol. 52 (24) (2018) 14371–14380, https://doi.org/10.1021/acs.est.8b05246.
[42] J. Li, B. Shen, Z. Hong, B. Lin, B. Gao, Y. Chen, A facile approach to synthesize novel oxygen-doped g-C3N4 with superior visible-light photoreactivity, Chem Commun (Camb) 48 (98) (2012) 12017–12019, https://doi.org/10.1039/c2cc35862j.
[43] D. Briggs, G. Beamson, XPS studies of the oxygen 1s and 2s levels in a wide range of functional polymers, Anal. Chem. 65 (11) (1993) 1517–1523.
[44] F. Wei, Y. Liu, H. Zhao, X. Ren, J. Liu, T. Hasan, L. Chen, Y. Li, B.L. Su, Oxygen self-doped g-C3N4 with tunable electronic band structure for unprecedentedly enhanced photocatalytic performance, Nanoscale 10 (9) (2018) 4515–4522, https://doi.org/10.1039/c7nr09660g.
[45] S. Wang, L. Xu, J. Wang, Enhanced activation of peroxymonosulfate through exfoliated oxygen-doping graphitic carbon nitride for degradation of organic pollutants, Chem. Eng. J. 428 (2022), 131066, https://doi.org/10.1016/j.cej.2021.131066.
[46] S. Zhang, Y. Liu, P. Gu, R. Ma, T. Wen, G. Zhao, L. Li, Y. Ai, C. Hu, X. Wang, Enhanced photodegradation of toxic organic pollutants using dual-oxygen-doped porous g-C3N4: Mechanism exploration from both experimental and DFT studies, Appl. Catal. B-Environ. 248 (2019) 1–10, https://doi.org/10.1016/j.apcatb.2019.02.008.
[47] J. Ran, T.Y. Ma, G. Gao, X.-W. Du, S.Z. Qiao, Porous P-doped graphitic carbon nitride nanosheets for synergistically enhanced visible-light photocatalytic H2 production, Energy Environ. Sci. 8 (12) (2015) 3708–3717, https://doi.org/10.1039/c5ee02650d.
[48] H. Bang Truong, B. The Huy, S. Kumar Ray, Y.-I. Lee, J. Cho, J. Hur, H2O2-assisted photocatalysis for removal of natural organic matter using nanosheet C3N4-WO3 composite under visible light and the hybrid system with ultrafiltration, Chem. Eng. J. 399 (2020), 125733, https://doi.org/10.1016/j.cej.2020.125733.
[49] Y. Shang, X. Chen, W. Liu, P. Tan, H. Chen, L. Wu, C. Ma, X. Xiong, J. Pan, Photocorrosion inhibition and high-efficiency photoactivity of porous g-C3N4/Ag2CrO4 composites by simple microemulsion-assisted co-precipitation method, Appl. Catal. B-Environ. 204 (2017) 78–88, https://doi.org/10.1016/j.apcatb.2016.11.025.
[50] L. Chen, D. Zhu, J. Li, X. Wang, J. Zhu, P.S. Francis, Y. Zheng, Sulfur and potassium co-doped graphitic carbon nitride for highly enhanced photocatalytic hydrogen evolution, Appl. Catal. B-Environ. 273 (2020), 119050, https://doi.org/10.1016/j.apcatb.2020.119050.
[51] H.-X. Fang, H. Guo, C.-G. Niu, C. Liang, D.-W. Huang, N. Tang, H.-Y. Liu, Y.-Y. Yang, L. Li, Hollow tubular graphitic carbon nitride catalyst with adjustable nitrogen vacancy: Enhanced optical absorption and carrier separation for improving photocatalytic activity, Chem. Eng. J. 402 (2020), 126185, https://doi.org/10.1016/j.cej.2020.126185.
[52] L. Chen, Y. Wang, S. Cheng, X. Zhao, J. Zhang, Z. Ao, C. Zhao, B. Li, S. Wang, S. Wang, H. Sun, Nitrogen defects/boron dopants engineered tubular carbon nitride for efficient tetracycline hydrochloride photodegradation and hydrogen evolution, Appl. Catal. B-Environ. 303 (2022), 120932, https://doi.org/10.1016/j.apcatb.2021.120932.
[53] P. Qiu, C. Xu, H. Chen, F. Jiang, X. Wang, R. Lu, X. Zhang, One step synthesis of oxygen doped porous graphitic carbon nitride with remarkable improvement of photo-oxidation activity: Role of oxygen on visible light photocatalytic activity, Appl. Catal. B-Environ. 206 (2017) 319–327, https://doi.org/10.1016/j.apcatb.2017.01.058.
[54] M. Kong, Y. Li, X. Chen, T. Tian, P. Fang, F. Zheng, X. Zhao, Tuning the relative concentration ratio of bulk defects to surface defects in TiO2 nanocrystals leads to high photocatalytic efficiency, J. Am. Chem. Soc. 133 (41) (2011) 16414–16417, https://doi.org/10.1021/ja207826q.
[55] Y. Zhao, J. Geng, X. Wang, X. Gu, S. Gao, Tetracycline adsorption on kaolinite: pH, metal cations and humic acid effects, Ecotoxicology 20 (5) (2011) 1141–1147, https://doi.org/10.1007/s10646-011-0665-6.
[56] A. Rincon, Effect of pH, inorganic ions, organic matter and H2O2 on E. coli K12 photocatalytic inactivation by TiO2Implications in solar water disinfection, Appl. Catal. B 51 (4) (2004) 283–302.
[57] P. Chen, L. Blaney, G. Cagnetta, J. Huang, B. Wang, Y. Wang, S. Deng, G. Yu, Degradation of Ofloxacin by Perylene Diimide Supramolecular Nanofiber Sunlight-Driven Photocatalysis, Environ. Sci. Technol. 53 (3) (2019) 1564–1575, https://doi.org/10.1021/acs.est.8b05827.
[58] M. Li, D. Liu, X. Chen, Z. Yin, H. Shen, A. Aiello, K.R. McKenzie Jr., N. Jiang, X. Li, M.J. Wagner, D.P. Durkin, H. Chen, D. Shuai, Radical-driven decomposition of graphitic carbon nitride nanosheets: light exposure matters, Environ. Sci. Technol. 55 (18) (2021) 12414–12423, https://doi.org/10.1021/acs.est.1c03804.
[59] X.D. Zhu, Y.J. Wang, R.J. Sun, D.M. Zhou, Photocatalytic degradation of tetracycline in aqueous solution by nanosized TiO2, Chemosphere 92 (8) (2013) 925–932, https://doi.org/10.1016/j.chemosphere.2013.02.066.
[60] G. Yang, Y. Liang, K. Wang, J. Yang, Z. Zeng, R. Xu, X. Xie, Simultaneous introduction of 0D Bi nanodots and oxygen vacancies onto 1D Bi6Mo2O15 sub-microwires for synergistically enhanced photocatalysis, Chem. Eng. J. 409 (2021), 128098, https://doi.org/10.1016/j.cej.2020.128098.